

Ternary-type Opacity and Hybrid Odometry for RGB-only NeRF-SLAM

Junru Lin^{1,2} Asen Nachkov¹ Songyou Peng³ Luc Van Gool^{1,3} Danda Pani Paudel^{1,3}

¹INSAIT, Sofia University

²University of Toronto

³ETH Zurich

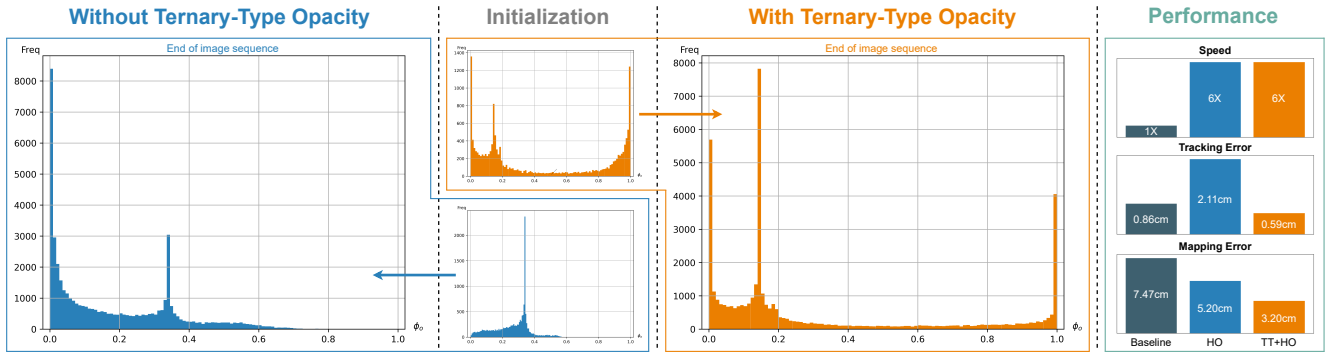


Figure 1. **Illustration of Ternary-type Opacity and Performance Comparison.** The baseline without (left) and our method with (middle) the ternary-type (TT) prior during SLAM initialization and the rest. The TT behaviour (middle) leads to improvements in both mapping and tracking performance (right), and the hybrid odometry (HO) method speeds up the baseline by 6 times (right). The proposed combination of TT+HO provides the best outcome (right). Results obtained on the Replica [35] *office-0*.

Abstract

The opacity of rigid 3D scenes with opaque surfaces is considered to be of a binary type. However, we observed that this property is not followed by the existing RGB-only NeRF-SLAM. Therefore, we are motivated to introduce this prior into the RGB-only NeRF-SLAM pipeline. Unfortunately, the optimization through the volumetric rendering function does not facilitate easy integration of the desired prior. Instead, we observed that the opacity of ternary-type (TT) is well supported. In this work, we study why ternary-type opacity is well-suited and desired for the task at hand. In particular, we provide theoretical insights into the process of jointly optimizing radiance and opacity through the volumetric rendering process. Through exhaustive experiments on benchmark datasets, we validate our claim and provide insights into the optimization process, which we believe will unleash the potential of RGB-only NeRF-SLAM. To foster this line of research, we also propose a simple yet novel visual odometry scheme that uses a hybrid combination of volumetric and warping-based image renderings. More specifically, the proposed hybrid odometry (HO) additionally uses image warping-based coarse odometry, leading up to an order of magnitude final speed-up. Furthermore, we show that the proposed TT and HO well comple-

ment each other, offering state-of-the-art results on benchmark datasets in terms of both speed and accuracy.

1. Introduction

The advent of Neural Radiance Fields (NeRF) [22] has marked a paradigm shift in 3D scene reconstruction methodologies. Therefore, several NeRF-based Simultaneous Localization and Mapping (SLAM) frameworks, referred here as NeRF-SLAM, have been developed recently [16, 32, 33, 36, 44, 50–53]. Most existing works use RGB-D sensors, which limits their ubiquitous use. This practical reason makes the RGB-only NeRF-SLAM of very high interest, which also offers dense mapping by its virtue. Despite the promises, many challenges still remain to fully realize RGB-only NeRF-SLAM.

Three separate noteworthy attempts for RGB-only NeRF-SLAM have been made in the literature: (i) NeRF-SLAM [32], (ii) DIM-SLAM [16], and (iii) NICER-SLAM [53]. Among them, NeRF-SLAM uses both pre-trained poses and depth networks, and NICER-SLAM uses pre-trained depth networks, making the underlying problems associated with the task at hand obscure. Note that we are interested in addressing the intrinsic challenges of RGB-

only NeRF-SLAM. In contrast, DIM-SLAM makes a more foundational approach, offering us a closer look at the intrinsic problems of our interests. Unfortunately though, we observed that DIM-SLAM is unstable even at the expense of impractically high computational budget¹. Nevertheless, we believe in the foundational approach of DIM-SLAM and therefore, we seek to find and address the remaining challenges to make RGB-only NeRF-SLAM practical, within a similar framework.

Our work primarily relies on the empirical observations obtained from our DIM-SLAM re-implementation. We carefully study and observe that the speed and performance rely on two major factors: (i) frame-wise volumetric rendering, and (ii) the failure to satisfy the binary-type opacity prior. Note that the opacity of rigid 3D scenes with opaque surfaces is considered to be of a binary type. However, we observed that this property is not followed. Unlike in the RGB-D case, where the rendered opacity is directly supervised using the depths, the RGB-only case exhibits a well-spread distribution, with almost non-existent high opacity which is illustrated in Figure 1 (left). As presumed, this is not a desired behaviour. Therefore, we are motivated to introduce this prior into the RGB-only NeRF-SLAM pipeline.

Our analysis of the volumetric rendering (VR) function reveals that the desired prior of binary-type opacity indeed is not easy to integrate and may not be necessary. Instead, the opacity of ternary-type (TT) is better suited for meaningful optimization. Intuitively, during VR any point behind another opaque point does not contribute to the rendered image. These points can have any opacity and radiance of their choice. Their spread, however, turns out to be hindering during the binary-type prior integration process. Therefore, we use a ternary-type model as illustrated in Figure 1 (middle), which leads to an improved performance, thanks to the prior of opaque 3D surfaces.

We avoid the frame-wise volumetric rendering during the camera tracking in SLAM. Instead, we propose to use a hybrid odometry (HO) technique that only uses image warping-based coarse camera localization during tracking. The finer adjustments of the camera odometry are performed during the bundle adjustment (BA) step, which is conducted jointly during the mapping process. The proposed hybrid odometry technique improves the speed up to an order of magnitude. This speed comes from the fact that the pose initialization required for BA can be obtained simply by minimizing the photometric error between the current image and the warped previous images using the rendered depths (of the so-far reconstructed implicit map), similar to the existing works [5, 6]. Note that this process avoids the VR altogether during the tracking process, yet the camera poses are still refined via volumetric rendering dur-

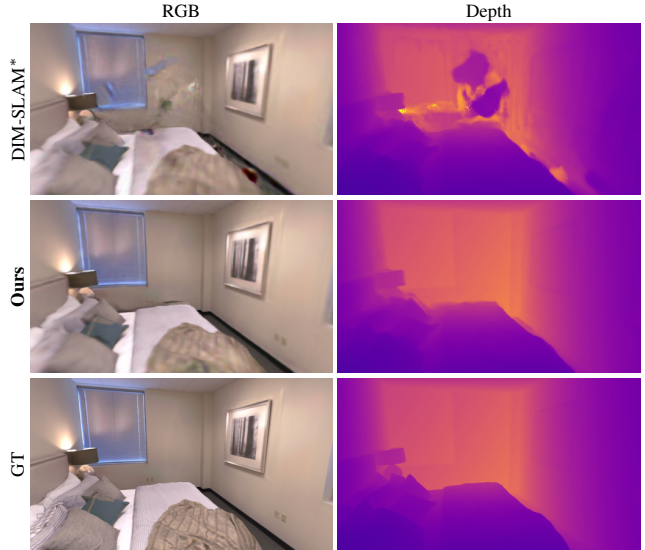


Figure 2. **Qualitative Results for Rendered RGB and Depth.** We show the rendered RGB and depth from a random pose after training the whole sequence of Replica [35] room-1. DIM-SLAM* refers to our re-implementation for DIM-SLAM [16].

ing the bundle adjustment. Furthermore, we show that the proposed ternary-type prior and the hybrid odometry technique complement each other, offering us state-of-the-art results on benchmark datasets in terms of both speed and accuracy, as illustrated in Figure 1 (right).

- Overall, our contributions are summarized as follows:
- We proposed a method to meaningfully exploit binary-type opacity prior of 3D surfaces by means of ternary-type modelling for the RGB-only NeRF-SLAM.
 - We provide detailed theoretical insights regarding the impact of volumetric rendering on mapping opaque 3D surfaces, by separating relevant and irrelevant parts.
 - The experimental results obtained by our method are very encouraging to fully realize RGB-only NeRF-SLAM.

2. Related Work

Visual SLAM. Simultaneous localization and mapping from 2D images is referred to as Visual SLAM [7]. Here, feature-based algorithms may estimate and track sparse or semi-dense keypoints across the image sequence [4], while direct methods may estimate the camera pose by minimizing a photometric error on the reconstruction [6, 21]. Common stages of each method include initialization, state prediction, tracking, and correction [3, 42, 43]. Different threads for mapping and tracking may be utilized [13, 28], and detection of loop closing may be further added [26, 27].

Neural Implicit Representations. More recently, neural radiance fields have emerged as an efficient method for

¹We re-implement DIM-SLAM as the implementation shared by the authors is not sufficient to reproduce the results reported in their paper.

high-quality scene mapping using neural networks [8, 22, 47]. Various improvements exist to reduce the requirements of accurate and/or known camera poses [11, 17, 40, 46], to improve training speed [9, 25, 37], to increase the scale of the reconstruction [38, 41], or to reduce the number of scene views [30, 48]. Additional works explore how to combine neural radiance fields with realistic outdoor [1, 31, 49] or degraded quality data suffering from blurring [14, 15, 19, 44], reduced illumination [23] or dynamic scenes [29].

SLAM with Neural Implicit Representations. A first line of work combines neural radiance fields with traditional SLAM systems and utilizes ground-truth depth to supervise the rendered point depth and to facilitate network training [12, 18, 24, 51]. iMAP [36] utilizes an MLP to represent the geometry of the scene and a keyframe graph to keep track of frames with significant novel information, uncorrelated to previous views. A follow-up work, NICE-SLAM [52], applies hierarchical feature grids with multiple MLPs so that it is able to capture larger and more complex scenes. Point-SLAM [33] instead uses a sparse set of neural points which are interpolated and weighted by the distance to the desired 3D point, and only sample several points near the depth along the ray using the known depth, resulting in better training efficiency.

Contrary to the work above, methods like [2, 16, 32, 53] do not rely on explicit depth supervision. NeRF-SLAM uses a pretrained Droid-SLAM [39] to get estimated poses and depth directly for the tracking frontend, and uses the CUDA-implemented Instant-NGP [25] to achieve fast map training. NICER-SLAM [53] uses a pretrained depth predictor and incorporates geometric cues based on RGB warping, optical flow, and surface normals, all implemented as additional loss terms. Different from [25, 53], DIM-SLAM [16] does not require any pretraining and relies on a photometric warping loss based on the structural similarity [45] to enforce the consistency of the geometry. However, due to per-frame bundle adjustment, the training speed of DIM-SLAM is very slow. Our work builds on DIM-SLAM and improves both the speed and the SLAM system performance.

3. Background

The standard SLAM pipeline consists of three key steps: (1) map initialization, (2) camera tracking, and (3) mapping and global optimization. We will delve into each of these aspects in Section 5. In the NeRF-based SLAM system, the map is represented using two neural functions for the implicit representation of opacity and the radiance of the scene, say $\phi_o(\cdot)$ and $\phi_c(\cdot)$, respectively. The radiance and opacity functions are optimized by using the image frames. More specifically, image frames are compared to the ren-

dered images, which are obtained by using the volumetric rendering process that involves $\phi_o(\cdot)$ and $\phi_c(\cdot)$ simultaneously. Let $\mathcal{S}_l = \{\mathbf{X}_i\}_{i=1}^n$ be an ordered set of 3D points along a ray l (emanating out and in front of the camera) that passes through the 2d-pixel \mathbf{x} . Then the rendered RGB value at \mathbf{x} is,

$$\mathbf{I}(\mathbf{x}) = \sum_{\mathbf{X}_i \in \mathcal{S}_l} w_i \phi_c(\mathbf{X}_i), \quad (1)$$

and the corresponding depth is rendered similarly,

$$D(\mathbf{x}) = \sum_{\mathbf{X}_i \in \mathcal{S}_l} w_i \phi_o(\mathbf{X}_i), \quad (2)$$

where the weights w_i are given by,

$$w_i = \phi_o(\mathbf{X}_i) \prod_{j=0}^{i-1} (1 - \phi_o(\mathbf{X}_j)). \quad (3)$$

We are interested in incorporating the prior for the opaque surfaces into the NeRF-SLAM system. Following the standard practice in NeRF [22], we use sigmoid functions to model the output activations of both $\phi_o(\cdot)$ and $\phi_c(\cdot)$. We are now ready to introduce our problem.

4. Ternary-type Opacity

Problem 4.1 *Recover the radiance field by minimizing the image reconstruction error between the ground-truth (GT) color c and rendered color, under an additional binary constraint on the weights, in the following form,*

$$\begin{aligned} & \underset{\phi, w_i}{\text{minimize}} \quad \left\| c - \sum_{\mathbf{X}_i \in \mathcal{S}_l} w_i \phi_c(\mathbf{X}_i) \right\|, \\ & \text{subject to} \quad w_i \in \{0, 1\}. \end{aligned} \quad (4)$$

Searching the radiance field ϕ_c by optimizing the problem formulation of Eq. (4) requires additional constraints on the weights w_i . In the NeRF setting, these weights are derived from the 3D opacity fields. Therefore, the constraint of Eq. (3) can be expressed as,

$$w_i = \phi_o(\mathbf{X}_i) \prod_{j=0}^{i-1} (1 - \phi_o(\mathbf{X}_j)) \in \{0, 1\}. \quad (5)$$

Lemma 4.2 *The desired weight constraints $w_i \in \{0, 1\}$ for the totally ordered set \mathcal{S}_l can be achieved if and only if at least one of the following statements is true,*

- i. $\phi_o(\mathbf{X}_i) = 0$.
- ii. $\phi_o(\mathbf{X}_j) = 1$ for some $\mathbf{X}_j \in \mathcal{S}_l$ with $j < i$.
- iii. $\phi_o(\mathbf{X}_i) = 1$ and $\phi_o(\mathbf{X}_j) = 0$ for all $j < i$.

Proof The forward proof is rather straightforward. The full proof is provided in the supp. materials. ■

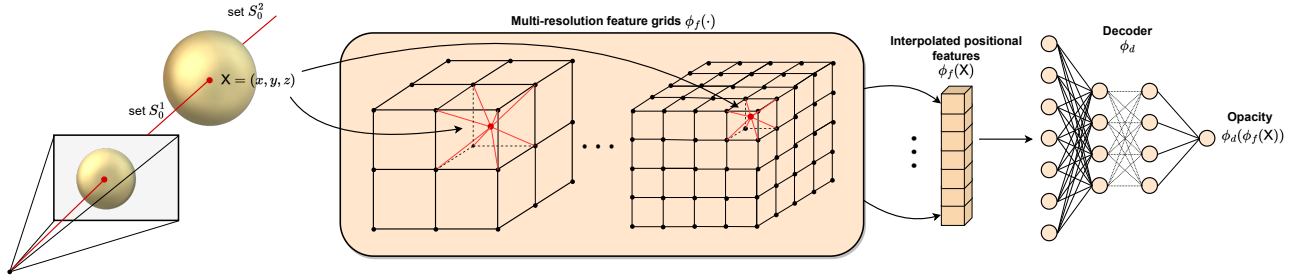


Figure 3. **Inferring the Opacity of a 3D Point.** We utilize a set of multi-resolution feature grids which we interpolate at the desired 3D point. The collected features are passed to a neural network to predict the color and the opacity. Only the opacity is shown for clarity.

Lemma 4.3 For any given optimal solution of the Problem 4.1, there exist nonenumerable sets of opacity measures $\mathcal{S}_o^* = \{\phi_o(X_i) | X_i \in \mathcal{S}_l\}$ leading to the same outcome.

Proof The proof is provided in the supp. materials. ■

Lemma 4.4 Any set $\mathcal{S}_o = \{\phi_o(X_i) \in \{0, 1\} | X_i \in \mathcal{S}_l\}$ that minimizes the objective of Eq. (4), is also a valid solution to the Problem 4.1.

Proof The proof is avoided as it is straightforward. ■

Theorem 4.5 (Relevant Binary-type Opacity) For an ordered set \mathcal{S}_o and ordered partition $\mathcal{S}_o = \{\mathcal{S}_o^1, \mathcal{S}_o^2\}$, let $\mathcal{S}_o^1 = \{X_k\}_{k=0}^i$. If \mathcal{S}_o^1 minimizes the objective of Eq. (4) with $\phi_o(X) \in \{0, 1\}$ for all $X \in \mathcal{S}_o^1$, except for X_i when $\phi_o(X) = 0$, then it is also a valid solution to Problem 4.1.

Proof The proof uses Lemmas 4.2, 4.3, and 4.4, which is provided in the supp. materials. ■

Note that in Theorem A.3, the irrelevant set \mathcal{S}_o^2 contributes neither to the objective nor to the constraint of the Problem 4.1. Therefore, we would like to avoid optimizing for \mathcal{S}_o^2 . Unfortunately though, we do not know the partition $\mathcal{S}_o = \{\mathcal{S}_o^1, \mathcal{S}_o^2\}$ beforehand. Furthermore, some members of \mathcal{S}_o^2 may contribute to the other pixels c_p . In either case, the eventual division between relevant and irrelevant sets with the very same properties (except the ordered subsets) can be made. Therefore, we develop the remaining paper using a single pixel-based formulation, involving a set \mathcal{S}_l over the corresponding ray, without losing the generality to the general sets in the 3D space.

In our experimental setting, initializing $\phi_o(X)$ to any value for any chosen X is possible. Therefore, we propose to initialize with a straightforward fixed value of all $X \in \mathcal{S}_l$. However, we find that some trivial initializations lead to undesired outcomes during the iterative optimization.

Proposition 4.6 Under the gray-world assumption, the initializations $\phi_o(X) = 0, \forall X \in \mathcal{S}_l$ or $\phi_o(X) = 1, \forall X \in \mathcal{S}_l$ are sub-optimal for iterative optimization of Problem 4.1.

Proof The proof (in supp. materials) relies on the observation that both initializations result in black images. ■

We resort to the map initialization step of the SLAM to initialize $\phi_o(\cdot)$. Before providing further details, we first present our decomposition of $\phi_o(\cdot)$, which is illustrated in Figure 3. To obtain the opacity of a 3D point X , we embed it into a feature vector $\phi_f(X)$, and then decode the feature vector into opacity using decoder $\phi_d(\cdot)$ such that $\phi_o(X) = \phi_d(\phi_f(X))$. During the map initialization, we learn the decoder $\phi_d(\cdot)$ which is later frozen, and only $\phi_f(\cdot)$ is optimized during the tracking and mapping process. In the latter stage, as we initialize all $\phi_f(\cdot)$ with a constant value η , for any point in the space that has not yet been optimized, it always has $\phi_f(\cdot)$ being η , and thus also keep the opacity to the initial value, denoted as o_{init} . Now, we are interested in addressing the following problem.

Problem 4.7 Optimize the objective function of Problem 4.1 such that $\phi_o(X) \in \{0, 1\}$ for all $X \in \mathcal{S}_o^1$, while fixing $\phi_o(X) = o_{init}$ for all the irrelevant part $X \in \mathcal{S}_o^2$.

Theorem 4.8 The solution to Problem 4.7 will optimize Problem 4.1 without violating the constraints and with the optimal transport for $|\mathcal{S}_o^2| \gg |\mathcal{S}_o^1|$.

Proof The proof is provided in the supp. materials. ■

To address Problem 4.7, a crucial unresolved matter involves dividing the set \mathcal{S}_o into subsets \mathcal{S}_o^1 and \mathcal{S}_o^2 . Unfortunately, this division cannot be known beforehand due to the nature of the SLAM pipeline. Notice that we wish to produce binary outputs for \mathcal{S}_o^1 and fixed value of o_{init} for \mathcal{S}_o^2 , in order to avoid unnecessary updates and thus make the process faster. On the other hand, imposing the prior of the necessary conditions on opacity (for binary weights) can lead to better solutions. To this end, we aim to model a softly-binarized decoder network $\phi_d(\cdot)$ during the map initialization stage. Learning this decoder jointly with $\phi_f(\cdot)$ allows us to choose o_{init} meaningfully. More specifically,

Algorithm 1 Ternary-type Opacity Optimization

1. During SLAM initialization:
 - Initialize $\phi_f(\cdot)$ such that all outputs are a chosen constant η .
 - Train $\phi_d(\cdot)$ jointly with $\phi_f(\cdot)$ for an optimal temperature τ .
 - Obtain the opacity initialization $o_{init} = \phi_d(\eta)$.
 2. During Mapping and Tracking:
 - For all \mathbf{X} that have not yet been updated, $\phi_o(\mathbf{X}) = o_{init}$ by default.
 - Use decoder $\phi_d(\cdot)$ with temperature τ to realize $\phi_o(\cdot)$.
-

during the joint optimization, we set $\eta = 0$ so that the outputs of $\phi_f(\cdot)$ are initialized to zero. The optimization process then automatically adjusts $\phi_d(0)$ for the scene, which also corresponds exactly to the irrelevant set \mathcal{S}_o^2 . Note that $\phi_f(\cdot)$ for \mathcal{S}_o^2 will be fixed to zeros, as they do not contribute to the optimization objective. Nevertheless, the value $\phi_d(0)$ changes in the initialization stage, after which it becomes fixed and is referred to as o_{init} .

Softly-binarized Decoder. To meet the desired criteria $\phi_d(\mathbf{X}) \in \{0, 1\}$ for all $\mathbf{X} \in \mathcal{S}_o^1$, we wish to binarize the decoder $\phi_d(\cdot)$ via an activation function. However, maintaining high-performance levels while binarizing activations is challenging. This challenge emerges from the reduced expressiveness of neurons due to restricted states and the introduction of discrete computational nodes, which hinder the propagation of gradients during training processes [20]. Therefore, we softly binarize the decoder $\phi_d(\cdot)$ by using the output activation of a continuous sigmoid function with temperature τ . We tune the temperature τ during the map initialization stage when o_{init} is also learned. To sum up, we initialize the opacities to o_{init} and encourage the opacities $\phi_o(\mathbf{X}) \in \mathcal{S}_o^1$ to be binary-type by using the softly-binarized sigmoid activation function with temperature τ . Consequently, the final opacity distribution is encouraged to be ternary-type which offers better results in our experiments, attributed to the incorporation of of real-world priors and volumetric rendering formulation. Our approach is outlined in Algorithm 1.

In our experiments, we follow the implementation of NICE-SLAM [52] and use the multi-scale grid-based representation of $\phi_f(\cdot)$. Such representation makes the realization of the Algorithm 1 straightforward. In fact, NICE-SLAM makes several design choices suitable for our algorithm, however without the motivation of modelling the ternary-type opacity distribution. We showcase the benefit of leveraging the prior of ternary-type opacity through exhaustive experiments.

5. Hybrid Odometry for NeRF-SLAM

5.1. SLAM System Design

Initialization. During the initialization, we take the first N_0 frames to train the color and opacity decoder, as well as the feature grid-based scene presentation and the camera poses. We take the ground truth of the camera poses for the first two frames, and estimate the following $(N_0 - 2)$ camera poses under the constant velocity motion model, where each camera pose is estimated from the previous two camera poses. The loss used in initialization is similar to the one in bundle adjustment, but each term is added after some iterations (see supp. materials for more details).

Hybrid Odometry. After initialization, the color and opacity decoders are fixed. We group the frames and perform hybrid odometry using gradient-based localization (GL) and bundle adjustment (BA). Each group has N frames, and thus the m -th group $\mathcal{G}_m = \{N_0 + (m - 1)N + i\}_{i=1}^N$. For notation, the 0-th group is defined as the frames used for the initialization, i.e., $\mathcal{G}_0 = \{i\}_{i=1}^{N_0}$. Note that the last group may have less than N frames, depending on the total number of frames in the sequence. We perform GL for each frame in order, and at the end of the group we perform BA for the whole group.

5.2. Gradient-based Localization by Warping

We track the camera frame by frame using GL by warping. For group \mathcal{G}_m , we take the last five frames from the previous group (i.e., $\{N_0 + (m - 1)N + i\}_{i=-4}^0$, denoted as \mathcal{T}) for tracking reference, and randomly sample P pixels from frames \mathcal{T} . For a sampled pixel \mathbf{x} with RGB value \mathbf{I}_x^g , we render its depth D_x with the estimated camera pose of its associated frame, and project it to 3D space with the depth:

$$\mathbf{X} = \mathbf{R}\mathbf{K}^{-1}[\mathbf{x}, 1]^\top D_x + \mathbf{t}, \quad (6)$$

where \mathbf{R} and \mathbf{t} are the camera poses associated to the pixel \mathbf{x} , \mathbf{K} is the known camera intrinsic matrix. In this manner, we form a set of 3D points, say $\mathcal{X} = \{\mathbf{X}_i\}_{i=1}^P$, which will be used as a reference for tracking all frames in \mathcal{G}_m .

For frame $i \in \mathcal{G}_m$, we first get an initial estimation of the camera pose with the constant velocity assumption, using the estimated camera poses $[\mathbf{R}_{i-2}, \mathbf{t}_{i-2}]$ and $[\mathbf{R}_{i-1}, \mathbf{t}_{i-1}]$, to get $[\mathbf{R}_i, \mathbf{t}_i]$. Then we optimize the camera pose using gradient-based localization by warping. In each optimization step, we project all points in \mathcal{X} to the image space of frame i :

$$\hat{\mathbf{x}} \sim \mathbf{K}\mathbf{R}_i^\top(\mathbf{X} - \mathbf{t}_i). \quad (7)$$

All the projected 2D points form a set $\hat{\mathcal{X}} = \{\hat{\mathbf{x}}|\mathbf{X} \in \mathcal{X}\}$, in which we filter out the points outside of the image boundaries to get $\hat{\mathcal{X}}_b \subseteq \hat{\mathcal{X}}$.

Finally, L1 loss can be calculated between the RGB value \mathbf{I}_x^g at original location \mathbf{x} and bilinearly interpolated

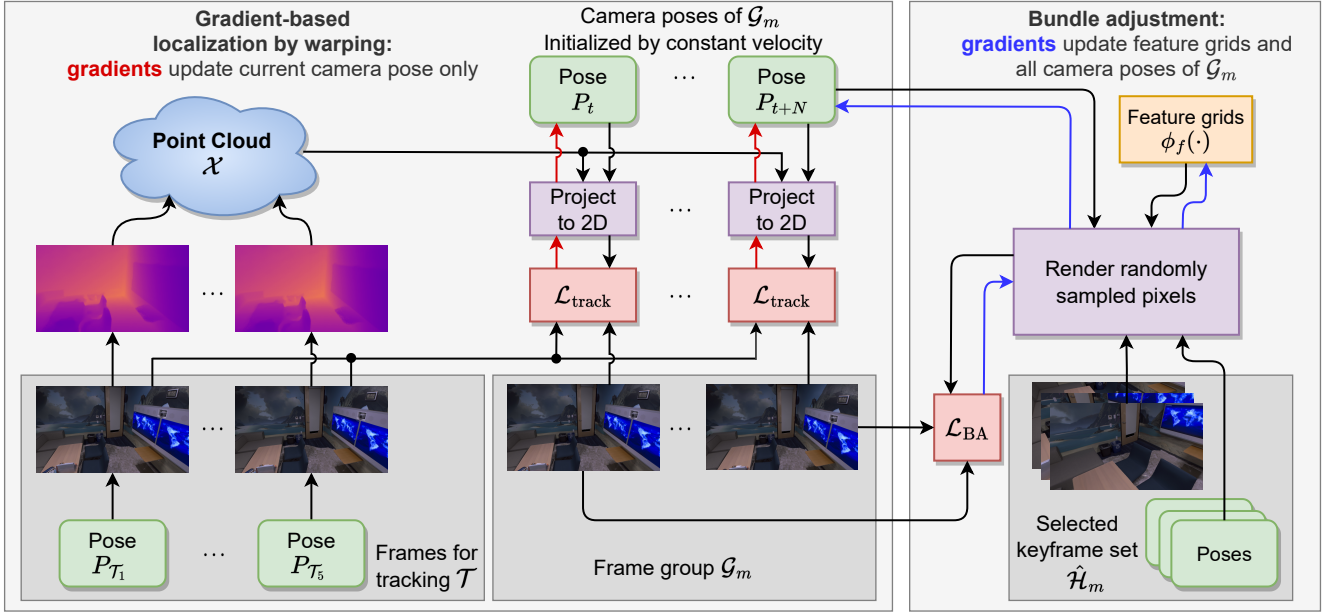


Figure 4. **Hybrid Odometry.** For simplicity t refers to the index of the first frame from the current frame group \mathcal{G}_m and T_1 is the first frame from the tracking frames. In **gradient-based localization by warping**, we initialize poses by constant velocity, render the depth for some pixels on the last few frames \mathcal{T} from the previous frame group to get point cloud \mathcal{X} , and update the camera poses by minimizing the reprojection loss of \mathcal{X} to the current frame \mathcal{G}_m . In **bundle adjustment** we select several keyframes and together with \mathcal{G}_m use volumetric rendering to produce pixel values. The loss is backpropagated to the feature grids and the camera poses belonging to frames in \mathcal{G}_m .

RGB value at projected location \hat{x} on current frame i , denoted as $\mathbf{I}_x^i(\cdot)$, which is a function of camera pose $[\mathbf{R}_i, \mathbf{t}_i]$. Considering all points in $\hat{\mathcal{X}}_b$, we define the tracking loss as:

$$\mathcal{L}_{\text{track}} = \sum_{\hat{x} \in \hat{\mathcal{X}}_b} \|\mathbf{I}_x^g - \mathbf{I}_x^i(\mathbf{R}_i, \mathbf{t}_i)\|_1, \quad (8)$$

Note that minimizing $\mathcal{L}_{\text{track}}$ improves the camera pose parameters. In this process, $\phi_o(\cdot), \phi_c(\cdot)$ using during the volumetric process not involved. This leads to a significant increase in the overall speed, since the volumetric rendering process is computationally expensive.

5.3. Bundle Adjustment

After all frames in group \mathcal{G}_m have their estimated camera poses optimized by gradient-based localization, they will be put together and used for joint optimization for the neural scene representation and the camera poses of \mathcal{G}_m .

Global Keyframe Set. To ensure the global consistency and awareness of the scene representation, we keep a global keyframe set. For frame group \mathcal{G}_m , its corresponding global keyframe set is

$$\mathcal{H}_m = \{1, 1 + H, 1 + 2H, \dots\} \subseteq \bigcup_{i=0}^{m-1} \mathcal{G}_i, \quad (9)$$

where H is the global keyframe frequency deciding how sparse \mathcal{H}_m is. As $|\mathcal{H}_m|$ increases with m increasing, for the computational efficiency, we only select a subset of \mathcal{H}_m for BA by an overlapping ratio. For each frame $h \in \mathcal{H}_m$, we randomly sample S pixels and render the depth to reproject them to frame, which is the last frame in \mathcal{G}_m , with \bar{S} pixels landing inside the image boundary. Then the overlapping ratio between frame h and $N_0 + mN$ can be estimated as:

$$r = \frac{\bar{S}}{S}. \quad (10)$$

We set a threshold R and randomly select L frames from \mathcal{H}_m with $r \geq R$, denoted as $\hat{\mathcal{H}}_m$.

Optimization. We have two sets of frames for BA: current frame group \mathcal{G}_m and selected global keyframe set $\hat{\mathcal{H}}_m$. We optimize both camera poses and feature grids in BA. However, only the camera poses of \mathcal{G}_m will be optimized, whereas the camera poses of $\hat{\mathcal{H}}_m$ will be fixed in the whole BA process. We denote the whole frame set used for BA as $\mathcal{B}_m = \mathcal{G}_m \cup \hat{\mathcal{H}}_m$.

For frame i in \mathcal{B}_m , we randomly sample Q pixels to get pixel set \mathcal{Q}_i . The photometric rendering loss is defined as:

$$\mathcal{L}_{\text{rgb}} = \sum_{i \in \mathcal{B}_m} \sum_{\mathbf{p} \in \mathcal{Q}_i} \|\mathbf{I}_{\mathbf{p}} - \hat{\mathbf{I}}_{\mathbf{p}}(\mathbf{R}_i, \mathbf{t}_i, \mathcal{F})\|_1, \quad (11)$$

where \mathbf{I}_p is the GT RGB value at pixel p , and $\hat{\mathbf{I}}_p(\cdot)$ is the rendered RGB value at pixel q , as a function of the camera pose $[\mathbf{R}_i, \mathbf{t}_i]$ and the set of features \mathcal{F} representing $\phi_f(\cdot)$.

Following DIM-SLAM [16], we further consider patch-based warping matches, for the purpose of geometric consistency. For each pixel $p \in Q_i$ from frame i , we expand it to several patches and denote the patch with size $z \times z$ as P_z , where $z \in Z$ and Z is the set of patch sizes. These patches are projected to 3D space with the rendered depth, and are then reprojected back to all other frames in \mathcal{B}_m . Those reprojected patches that land inside the frame boundaries are considered valid, and we drop patches with less than 5 valid reprojections. The patch-based warping loss for all frames and their sampled pixels is defined as:

$$\mathcal{L}_{\text{warping}} = \sum_{i \in \mathcal{B}_m} \sum_{p \in Q_i} \sum_{z \in Z} \alpha_z \mathcal{L}_{\text{SSIM}}(P_z, i), \quad (12)$$

where α_z is the loss scalar for patch size z . In the formula above, the structure similarity loss [45] function $\mathcal{L}_{\text{SSIM}}$ takes a patch and its associated frame id as input, and is defined as:

$$\mathcal{L}_{\text{SSIM}}(P, i) = \sum_{j \in \mathcal{B}_m, j \neq i} \text{SSIM}(\mathbf{I}_P, \hat{\mathbf{I}}_P(\mathbf{R}_j, \mathbf{t}_j, R_j, \mathcal{F})), \quad (13)$$

where \mathbf{I}_P is the GT RGB values for patch P , and $\hat{\mathbf{I}}_P$ is the reprojected patch P from frame i to frame j , as a function of camera poses $[\mathbf{R}_i, \mathbf{t}_i]$ and $[\mathbf{R}_j, \mathbf{t}_j]$, as well as the feature representation set \mathcal{F} . Finally, the total loss for BA is the scaled sum of the photometric loss and geometric loss:

$$\mathcal{L}_{\text{BA}} = \alpha_{\text{rgb}} \mathcal{L}_{\text{rgb}} + \alpha_{\text{warping}} \mathcal{L}_{\text{warping}}, \quad (14)$$

where α_{rgb} and α_{warping} are scalars. Minimizing the loss \mathcal{L}_{BA} helps both camera localization and scene mapping, by improving the camera poses and feature grids.

6. Experiments

In this section, we provide abundant experiments showcasing the benefits of our proposed ternary-type opacity and hybrid odometry.

6.1. Implementation Details

Baseline. For the DIM-SLAM baseline, we re-implement the code, adapting the incomplete code released by the authors, and all hyper-parameters are set similarly to our settings. We notice that NICER-SLAM also re-implemented DIM-SLAM and reported results in their paper, and thus we take some of the results for fair comparison.

Setup. We use 7 layers of multi-resolution feature grids, similar to [16], the sizes of which are set differently for different datasets. materials. We experiment with the influence

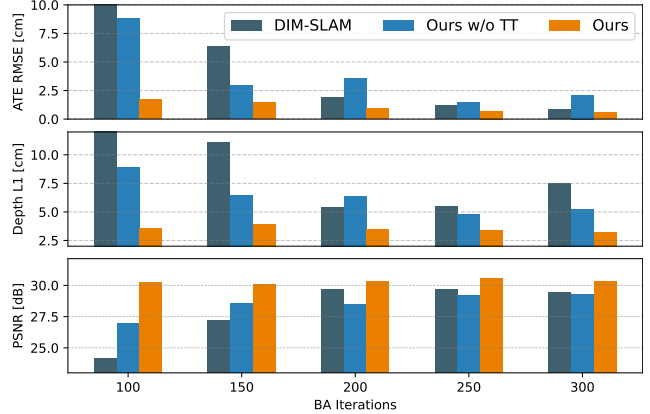


Figure 5. **Ablation Study.** We evaluate final results for both tracking and mapping performance on Replica *office-0*, with different numbers of iterations in BA. ‘TT’ denotes ternary-type opacity. While DIM-SLAM [16] has a poor performance when we decrease the BA iterations, our method is able to maintain the performance while running fewer iterations and performing BA every ten frames. This indicates that TT contributes to map training convergence speed and the system robustness.

of sigmoid temperature τ on Replica *office-0* (details provided in supp. materials) and choose 10 for both color and density. For the initialization, we set the frame number $N_0 = 15$ and train for 1500 iterations. We set the following group size $N = 10$. For GL, we sample $P = 10000$ pixels in the tracking frame set \mathcal{T} and optimize the camera poses for 200 iterations. For BA, we take the global keyframe frequency $H = 5$, we select $L = 10$ frames from the global keyframe set with the overlapping threshold $R = 0.1$, and run for 300 iterations. For the learning rates, please refer to the supplementary materials.

We build on the code released by DIM-SLAM. With a straightforward PyTorch implementation, on average each iteration in GL takes about 6ms and each iteration in BA takes about 145ms on a single NVIDIA A100 GPU.

Datasets. We evaluate our method on synthetic dataset Replica [35] and real-world dataset 7-Scenes [10, 34]. For Replica, we set the multi-resolution voxel sizes to $\{0.64, 0.48, 0.32, 0.24, 0.16, 0.12, 0.08\}$ m, and sample $Q = 3000$ pixels in BA. Using more than that amount of pixels yields marginal accuracy improvements at an increasing computational cost. For more challenging dataset 7-Scenes, we set the finer multi-resolution feature grids with sizes $\{0.48, 0.32, 0.24, 0.16, 0.12, 0.08, 0.04\}$ m, and sample $Q = 5000$ pixels in BA. We run our method with $N = 10$ for all the scenes except for *kitchen*, which we find to be challenging and thus we use $N = 1$.

Evaluation of Tracking and Mapping. For the tracking performance, We report the tracking performance by evaluating the RMSE of Absolute Trajectory Error (ATE RMSE).

	Replica [35]								7-Scenes [34]						
	o-0	o-1	o-2	o-3	o-4	r-0	r-1	r-2	chess	fire	heads	kitchen	office	pumpkin	stairs
NICE-SLAM [†] [52]	0.99	0.90	1.39	3.97	3.08	1.69	2.04	1.55	2.16	1.63	7.80	5.73	19.34	3.31	4.31
NICER-SLAM [53]	2.12	3.23	2.12	1.42	2.01	1.36	1.60	1.14	3.28	6.85	4.16	3.94	10.84	20.00	10.81
NeRF-SLAM [†] [32]	12.75	10.34	14.52	20.32	14.96	17.26	11.94	15.76	9.34	8.57	4.44	9.02	16.67	43.96	5.41
DIM-SLAM [†] [16]	0.43	0.26	0.65	0.55	3.69	1.06	0.49	0.32	60.13	2.41	39.42	39.11	24.15	13.07	10.45
DIM-SLAM*	0.86	0.47	3.50	1.95	30.39	80.16	10.10	27.48	5.22	9.61	8.01	29.92	9.76	17.12	12.83
Ours	0.59	1.74	1.70	0.81	3.47	4.51	0.91	7.49	4.86	6.00	6.30	7.14	14.14	18.73	12.40

Table 1. **Camera Tracking Results on Replica and 7-Scenes.** ATE RMSE [cm] (\downarrow) is used as the evaluation metric. o-x and r-x denote office-x and room-x respectively in Replica [35]. DIM-SLAM[†], NICE-SLAM[†] and NeRF-SLAM[†] are taken from NICER-SLAM [53], and DIM-SLAM* is the re-implementation by us. The methods in the upper section of the table utilize either GT depth or pseudo depth, whereas those in the lower section do not use any depth information.

	o-0	o-1	o-2	o-3	o-4	r-0	r-1	r-2
iMAP [†] [36]	(6.43, 7.39)	(7.41, 11.89)	(14.23, 8.12)	(8.68, 5.62)	(6.80, 5.98)	(5.70, 5.66)	(4.93, 5.31)	(6.94, 5.64)
NICE-SLAM [†] [52]	(1.51, 22.44)	(0.93, 25.22)	(8.41, 22.79)	(10.48, 22.94)	(2.43, 24.72)	(2.53, 29.90)	(3.45, 29.12)	(2.93, 19.80)
NeRF-SLAM [32]	(2.97, 34.90)	(1.98, 53.44)	(9.13, 39.30)	(10.58, 38.63)	(3.59, 39.21)	(2.97, 34.90)	(2.63, 36.95)	(2.58, 40.75)
DIM-SLAM* [16]	(7.47, 29.44)	(6.52, 30.48)	(18.35, 20.28)	(24.79, 19.93)	(37.45, 18.84)	(87.23, 8.97)	(23.74, 20.76)	(33.55, 20.32)
Ours	(3.20, 30.34)	(2.15, 31.67)	(10.43, 23.05)	(11.76, 23.32)	(13.23, 26.19)	(11.86, 21.22)	(4.79, 26.29)	(20.95, 22.54)

Table 2. **Geometric (L1) and Photometric (PSNR) results on Replica.** The pair of numbers denotes Depth L1 [cm] (\downarrow) and PSNR [dB] (\uparrow), respectively. iMAP[†] and NICE-SLAM[†] are taken from NeRF-SLAM, and DIM-SLAM* is our re-implementation.

	ATE RMSE [cm] \downarrow	Depth L1 [cm] \downarrow	PSNR [dB] \uparrow
w/o TT, HO	70.00	47.95	16.57
w/o HO	40.95	55.62	19.59
w/o TT	2.11	5.20	29.27
Ours	0.59	3.20	30.34

Table 3. **Ablation Study.** ‘TT’ and ‘HO’ denote ternary-type opacity and hybrid odometry respectively. Results obtained on Replica [35] office-0.

Following DIM-SLAM [16], we align the estimated trajectory with the ground truth and make scale corrections. For the mapping performance, we evaluate the geometric and photometric quality of Replica [35], following NeRF-SLAM [32]. After the whole sequence training, we render the depth and RGB for all frames using the estimated camera poses. For the geometric evaluation, we rescale the estimated depth to the GT depth, and filter out outliers by removing the pixels with a depth difference greater than 1m with GT depth. Subsequently, we take the mean of L1 loss between the GT depth and the rendered depth. For the photometric evaluation, we take PSNR between the rendered RGB images and the GT RGB images. The final reported L1 loss and PSNR are averaged from all frames.

6.2. Ablation Study

Effectiveness of Ternary-type Opacity. Table 3 showcases the enhanced performance in both mapping and tracking with ternary-type opacity. Furthermore, in Figure 5, we illustrate our ternary-type opacity enables a reduction in the

number of iterations in BA, with a minimal decrease in performance compared to DIM-SLAM.

Effectiveness of Hybrid Odometry. With our ternary-type opacity, we compare the tracking accuracy with and without using hybrid odometry, specifically employing camera poses derived from the constant velocity model without further optimization. As indicated in Table 3, using HO is crucial for achieving favorable mapping and tracking results.

7. Conclusion

We present a method for RGB-only NeRF-SLAM that benefits from the prior of the opaque scenes. This is achieved by the ternary-type modelling of the 3D scenes. Furthermore, we propose a hybrid method to estimate the camera motion that leads to a significant increase in overall speed. The theoretical insights that we provide in analyzing the volumetric rendering and opaque surfaces, in our context, is well supported by our experimental results. In fact, the reported observation has led us to propose a simple yet very effective strategy to exploit the opaque surface prior, which in turn offers us both improved accuracy and speed, thanks to the faster convergence offered by the proposed ternary-type prior.

Limitations and Future Work. While being online, the proposed method is not yet real-time on the consumer devices for many common applications. This requirements may be addressed by application- and hardware-specific code optimization and the system configurations, which remains as the future works.

References

- [1] Jonathan T Barron, Ben Mildenhall, Dor Verbin, Pratul P Srinivasan, and Peter Hedman. Mip-nerf 360: Unbounded anti-aliased neural radiance fields. In *CVPR*, 2022. 3
- [2] Chi-Ming Chung, Yang-Che Tseng, Ya-Ching Hsu, Xiang-Qian Shi, Yun-Hung Hua, Jia-Fong Yeh, Wen-Chin Chen, Yi-Ting Chen, and Winston H Hsu. Orbeez-slam: A real-time monocular visual slam with orb features and nerf-realized mapping. In *ICRA*, 2023. 3
- [3] Andrew J Davison, Ian D Reid, Nicholas D Molton, and Olivier Stasse. Monoslam: Real-time single camera slam. *IEEE TPAMI*, 2007. 2
- [4] Jakob Engel, Thomas Schöps, and Daniel Cremers. Lsd-slam: Large-scale direct monocular slam. In *ECCV*, 2014. 2
- [5] Jakob Engel, Jörg Stückler, and Daniel Cremers. Large-scale direct slam with stereo cameras. In *IROS*, 2015. 2
- [6] Jakob Engel, Vladlen Koltun, and Daniel Cremers. Direct sparse odometry. *IEEE TPAMI*, 2017. 2
- [7] Juan-Antonio Fernández-Madrigal. *Simultaneous Localization and Mapping for Mobile Robots: Introduction and Methods: Introduction and Methods*. IGI global, 2012. 2
- [8] Kyle Gao, Yina Gao, Hongjie He, Dening Lu, Linlin Xu, and Jonathan Li. Nerf: Neural radiance field in 3d vision, a comprehensive review. *arXiv preprint arXiv:2210.00379*, 2022. 3
- [9] Stephan J Garbin, Marek Kowalski, Matthew Johnson, Jamie Shotton, and Julien Valentin. Fastnerf: High-fidelity neural rendering at 200fps. In *ICCV*, 2021. 3
- [10] Ben Glocker, Shahram Izadi, Jamie Shotton, and Antonio Criminisi. Real-time rgb-d camera relocalization. In *ISMAR*, 2013. 7
- [11] Yoonwoo Jeong, Seokjun Ahn, Christopher Choy, Anima Anandkumar, Minsu Cho, and Jaesik Park. Self-calibrating neural radiance fields. In *ICCV*, 2021. 3
- [12] Mohammad Mahdi Johari, Camilla Carta, and François Fleuret. Eslam: Efficient dense slam system based on hybrid representation of signed distance fields. In *CVPR*, 2023. 3
- [13] Georg Klein and David Murray. Parallel tracking and mapping for small ar workspaces. In *ISMAR*, 2007. 2
- [14] Dogyoon Lee, Minhyeok Lee, Chajin Shin, and Sangyoun Lee. Dp-nerf: Deblurred neural radiance field with physical scene priors. In *CVPR*, 2023. 3
- [15] Dongwoo Lee, Jeongtaek Oh, Jaesung Rim, Sunghyun Cho, and Kyoung Mu Lee. Exblurf: Efficient radiance fields for extreme motion blurred images. In *ICCV*, 2023. 3
- [16] Heng Li, Xiaodong Gu, Weihao Yuan, Luwei Yang, Zilong Dong, and Ping Tan. Dense rgb slam with neural implicit maps. *arXiv preprint arXiv:2301.08930*, 2023. 1, 2, 3, 7, 8, 6
- [17] Chen-Hsuan Lin, Wei-Chiu Ma, Antonio Torralba, and Simon Lucey. Barf: Bundle-adjusting neural radiance fields. In *ICCV*, 2021. 3
- [18] Daniil Lisus, Connor Holmes, and Steven Waslander. Towards open world nerf-based slam. In *CRV*, 2023. 3
- [19] Li Ma, Xiaoyu Li, Jing Liao, Qi Zhang, Xuan Wang, Jue Wang, and Pedro V Sander. Deblur-nerf: Neural radiance fields from blurry images. In *CVPR*, 2022. 3
- [20] Siming Ma, David Brooks, and Gu-Yeon Wei. A binary-activation, multi-level weight rnn and training algorithm for adc-/dac-free and noise-resilient processing-in-memory inference with envm. *arXiv preprint arXiv:1912.00106*, 2019. 5
- [21] Andréa Macario Barros, Maugan Michel, Yoann Moline, Gwenolé Corre, and Frédéric Carrel. A comprehensive survey of visual slam algorithms. *Robotics*, 11(1):24, 2022. 2
- [22] Ben Mildenhall, Pratul P Srinivasan, Matthew Tancik, Jonathan T Barron, Ravi Ramamoorthi, and Ren Ng. Nerf: Representing scenes as neural radiance fields for view synthesis. In *ECCV*, 2020. 1, 3
- [23] Ben Mildenhall, Peter Hedman, Ricardo Martin-Brualla, Pratul P Srinivasan, and Jonathan T Barron. Nerf in the dark: High dynamic range view synthesis from noisy raw images. In *CVPR*, 2022. 3
- [24] Yuhang Ming, Weicai Ye, and Andrew Calway. idf-slam: End-to-end rgb-d slam with neural implicit mapping and deep feature tracking. *arXiv preprint arXiv:2209.07919*, 2022. 3
- [25] Thomas Müller, Alex Evans, Christoph Schied, and Alexander Keller. Instant neural graphics primitives with a multi-resolution hash encoding. *ACM Transactions on Graphics (ToG)*, 41(4):1–15, 2022. 3
- [26] Raul Mur-Artal and Juan D Tardós. Orb-slam2: An open-source slam system for monocular, stereo, and rgb-d cameras. *TRO*, 2017. 2
- [27] Raul Mur-Artal, Jose Maria Martinez Montiel, and Juan D Tardos. Orb-slam: a versatile and accurate monocular slam system. *TRO*, 2015. 2
- [28] Richard A Newcombe, Steven J Lovegrove, and Andrew J Davison. Dtam: Dense tracking and mapping in real-time. In *ICCV*, 2011. 2
- [29] Albert Pumarola, Enric Corona, Gerard Pons-Moll, and Francesc Moreno-Noguer. D-nerf: Neural radiance fields for dynamic scenes. In *CVPR*, 2021. 3
- [30] Daniel Rebain, Mark Matthews, Kwang Moo Yi, Dmitry Lagun, and Andrea Tagliasacchi. Lolnerf: Learn from one look. In *CVPR*, 2022. 3
- [31] Konstantinos Rematas, Andrew Liu, Pratul P Srinivasan, Jonathan T Barron, Andrea Tagliasacchi, Thomas Funkhouser, and Vittorio Ferrari. Urban radiance fields. In *CVPR*, 2022. 3
- [32] Antoni Rosinol, John J Leonard, and Luca Carlone. Nerf-slam: Real-time dense monocular slam with neural radiance fields. *arXiv preprint arXiv:2210.13641*, 2022. 1, 3, 8
- [33] Erik Sandström, Yue Li, Luc Van Gool, and Martin R Oswald. Point-slam: Dense neural point cloud-based slam. In *ICCV*, 2023. 1, 3
- [34] Jamie Shotton, Ben Glocker, Christopher Zach, Shahram Izadi, Antonio Criminisi, and Andrew Fitzgibbon. Scene coordinate regression forests for camera relocalization in rgb-d images. In *CVPR*, 2013. 7, 8

- [35] Julian Straub, Thomas Whelan, Lingni Ma, Yufan Chen, Erik Wijmans, Simon Green, Jakob J Engel, Raul Mur-Artal, Carl Ren, Shobhit Verma, et al. The replica dataset: A digital replica of indoor spaces. *arXiv preprint arXiv:1906.05797*, 2019. 1, 2, 7, 8, 3, 4, 5, 6
- [36] Edgar Sucar, Shikun Liu, Joseph Ortiz, and Andrew J Davison. imap: Implicit mapping and positioning in real-time. In *ICCV*, 2021. 1, 3, 8
- [37] Cheng Sun, Min Sun, and Hwann-Tzong Chen. Direct voxel grid optimization: Super-fast convergence for radiance fields reconstruction. In *CVPR*, 2022. 3
- [38] Matthew Tancik, Vincent Casser, Xinchun Yan, Sabeek Pradhan, Ben Mildenhall, Pratul P Srinivasan, Jonathan T Barron, and Henrik Kretzschmar. Block-nerf: Scalable large scene neural view synthesis. In *CVPR*, 2022. 3
- [39] Zachary Teed and Jia Deng. Droid-slam: Deep visual slam for monocular, stereo, and rgb-d cameras. In *NeurIPS*, 2021. 3
- [40] Prune Truong, Marie-Julie Rakotosaona, Fabian Manhardt, and Federico Tombari. Sparf: Neural radiance fields from sparse and noisy poses. In *CVPR*, 2023. 3
- [41] Haithem Turki, Deva Ramanan, and Mahadev Satyanarayanan. Mega-nerf: Scalable construction of large-scale nerfs for virtual fly-throughs. In *CVPR*, 2022. 3
- [42] Bastien Vincke, Abdelhafid Elouardi, and Alain Lambert. Design and evaluation of an embedded system based slam applications. In *2010 IEEE/SICE International Symposium on System Integration*, pages 224–229. IEEE, 2010. 2
- [43] Bastien Vincke, Abdelhafid Elouardi, Alain Lambert, and Alain Merigot. Efficient implementation of ekf-slam on a multi-core embedded system. In *IECON 2012-38th Annual Conference on IEEE Industrial Electronics Society*, pages 3049–3054. IEEE, 2012. 2
- [44] Peng Wang, Lingzhe Zhao, Ruijie Ma, and Peidong Liu. Bad-nerf: Bundle adjusted deblur neural radiance fields. In *CVPR*, 2023. 1, 3
- [45] Zhou Wang, Alan C Bovik, Hamid R Sheikh, and Eero P Simoncelli. Image quality assessment: from error visibility to structural similarity. *TIP*, 2004. 3, 7
- [46] Zirui Wang, Shangzhe Wu, Weidi Xie, Min Chen, and Victor Adrian Prisacariu. Nerf-: Neural radiance fields without known camera parameters. *arXiv preprint arXiv:2102.07064*, 2021. 3
- [47] Yiheng Xie, Towaki Takikawa, Shunsuke Saito, Or Litany, Shiqin Yan, Numair Khan, Federico Tombari, James Tompkin, Vincent Sitzmann, and Srinath Sridhar. Neural fields in visual computing and beyond. In *CGF*, 2022. 3
- [48] Alex Yu, Vickie Ye, Matthew Tancik, and Angjoo Kanazawa. pixelnerf: Neural radiance fields from one or few images. In *CVPR*, 2021. 3
- [49] Jason Zhang, Gengshan Yang, Shubham Tulsiani, and Deva Ramanan. Ners: Neural reflectance surfaces for sparse-view 3d reconstruction in the wild. In *NeurIPS*, 2021. 3
- [50] Wei Zhang, Tiecheng Sun, Sen Wang, Qing Cheng, and Norbert Haala. Hi-slam: Monocular real-time dense mapping with hybrid implicit fields. *arXiv preprint arXiv:2310.04787*, 2023. 1
- [51] Youmin Zhang, Fabio Tosi, Stefano Mattoccia, and Matteo Poggi. Go-slam: Global optimization for consistent 3d instant reconstruction. In *ICCV*, 2023. 3
- [52] Zihan Zhu, Songyou Peng, Viktor Larsson, Weiwei Xu, Hujun Bao, Zhaopeng Cui, Martin R Oswald, and Marc Pollefeys. Nice-slam: Neural implicit scalable encoding for slam. In *CVPR*, 2022. 3, 5, 8
- [53] Zihan Zhu, Songyou Peng, Viktor Larsson, Zhaopeng Cui, Martin R Oswald, Andreas Geiger, and Marc Pollefeys. Nicer-slam: Neural implicit scene encoding for rgb slam. *arXiv preprint arXiv:2302.03594*, 2023. 1, 3, 8

Ternary-type Opacity and Hybrid Odometry for RGB-only NeRF-SLAM

Supplementary Material

In this document, we provide the remaining proofs from Section 4, followed by the detailed implementation details and the full ablation study on the Replica dataset. Furthermore, several qualitative results are provided along with discussions.

Appendix A. Proof

Here we re-state the previous lemmas, propositions, and theorems before providing their remaining proofs.

Lemma A.1 (Lemma 4.2 in the paper) *The desired weight constraints $w_i \in \{0, 1\}$ for the totally ordered set \mathcal{S}_l can be achieved if and only if at least one of the following statements is true,*

- i. $\phi_o(\mathbf{X}_i) = 0$.
- ii. $\phi_o(\mathbf{X}_j) = 1$ for some $\mathbf{X}_j \in \mathcal{S}_l$ with $j < i$.
- iii. $\phi_o(\mathbf{X}_i) = 1$ and $\phi_o(\mathbf{X}_j) = 0$ for all $j < i$.

Proof Notice that $\phi_o(\mathbf{X}) \in [0, 1]$, which is a bounded interval. For forward case, $w_i = \phi_o(\mathbf{X}_i) \prod_{j=0}^{i-1} (1 - \phi_o(\mathbf{X}_j))$ results in $w_i \in \{0, 1\}$ with cases (i), (ii), and (iii), which can be verified by computations leading to $w_i = 0$ for (i), $w_i = 0$ for (ii), and $w_i = 1$ of (iii). The intermediate and final outcomes are summarized in Table 4:

Case	$\phi_o(\mathbf{X}_i)$	$\prod_{j=0}^{i-1} (1 - \phi_o(\mathbf{X}_j))$	w_i
(i)	0	–	0
(ii)	–	0	0
(iii)	1	1	1

Table 4. Three cases of binary weights w_i .

Now we provide the backward proof using the table above. As shown in case (i), all cases with $\phi_o(\mathbf{X}_i) = 0$ are already covered. On the other hand, when $\phi_o(\mathbf{X}_i) < 1$, the weights become $w_i < 1$, as $\prod_{j=0}^{i-1} (1 - \phi_o(\mathbf{X}_j)) \leq 1$. This leads to the only $w_i = 0$ choice to be taken, with $\prod_{j=0}^{i-1} (1 - \phi_o(\mathbf{X}_j)) = 0$ being possible only if case (ii) is satisfied. Similarly, when $\phi_o(\mathbf{X}_i) = 1$, $w_i \in \{0, 1\}$ is possible only with $\prod_{j=0}^{i-1} (1 - \phi_o(\mathbf{X}_j)) \in \{0, 1\}$. Under this condition, $\prod_{j=0}^{i-1} (1 - \phi_o(\mathbf{X}_j)) = 0$ leads to case (ii), whereas $\prod_{j=0}^{i-1} (1 - \phi_o(\mathbf{X}_j)) = 1$ leads to the case (iii). We exhausted all possibilities for $w_i \in \{0, 1\}$, all of them leading to the listed three statements. ■

Lemma A.2 (Lemma 4.3 in the paper) *For any given optimal solution of the Problem 4.1, there exist nonnumerable sets of opacity measures $\mathcal{S}_o^* = \{\phi_o(\mathbf{X}_i) | \mathbf{X}_i \in \mathcal{S}_l\}$ leading to the same outcome.*

Proof The proof relies on the fact that some variables involved, specifically some $\phi_o(\mathbf{X}_i)$, influence neither the objective function nor the constraints. For the sake of simplicity and sufficiency, we provide the proof from the point of view of an additional point having freedom to have nonnumerable possibilities, without affecting the the discussed objective and the constraints. In any general setting, any $w_i \in \{0, 1\}$ arising by satisfying any of the statements of Lemma A.1 may have arisen with a different setting of $\phi_o(\mathbf{X}_i)$. These are exactly the possibilities not covered by the statements in Lemma A.1. Now it is straightforward to see that the possibilities not covered by the statements in Lemma A.1 are indeed nonnumerable. This leads to the nonnumerable sets of opacity measures $\mathcal{S}_o^* = \{\phi_o(\mathbf{X}_i) | \mathbf{X}_i \in \mathcal{S}_l\}$ with the same outcome. ■

Theorem A.3 (Relevant Binary-type Opacity) *For an ordered set \mathcal{S}_o and ordered partition $\mathcal{S}_o = \{\mathcal{S}_o^1, \mathcal{S}_o^2\}$, let $\mathcal{S}_o^1 = \{\mathbf{X}_k\}_{k=0}^i$. If \mathcal{S}_o^1 minimizes the objective of Eq. (4) with $\phi_o(\mathbf{X}) \in \{0, 1\}$ for all $\mathbf{X} \in \mathcal{S}_o^1$, except for \mathbf{X}_i when $\phi_o(\mathbf{X}) = 0$, then it is also a valid solution to Problem 4.1.*

Proof When the objective of Equation (4) is minimized, it is sufficient to show that satisfying $\phi_o(\mathbf{X}) \in \{0, 1\}$ for all $\mathbf{X} \in \mathcal{S}_o^1$ is equivalent to satisfying the constraints of the Equation (4). This requires close observation that for any w_i , \mathcal{S}_o^1 is partitioned such that $\mathcal{S}_o^1 = \{\mathbf{X}_k\}_{k=0}^i$. When $\phi_o(\mathbf{X}) \in \{0, 1\}$ for all $\mathbf{X} \in \mathcal{S}_o^1$, it essentially leads to case (ii) of Lemma A.1 (please refer to the intermediate lemmas for notation developments) when $\phi_o(\mathbf{X}) = 1$ for any $\mathbf{X} \in \mathcal{S}_o^1$. Otherwise, it leads to case (iii) when for all $\mathbf{X} \in \mathcal{S}_o^1$, except for \mathbf{X}_i , $\phi_o(\mathbf{X}) = 0$. ■

Proposition A.4 (Proposition 4.6 in the paper)

Under the gray-world assumption, the initializations $\phi_o(\mathbf{X}) = 0, \forall \mathbf{X} \in \mathcal{S}_l$ or $\phi_o(\mathbf{X}) = 1, \forall \mathbf{X} \in \mathcal{S}_l$ are sub-optimal for iterative optimization of Problem 4.1.

Proof When $\phi_o(\mathbf{X}) = 0, \forall \mathbf{X} \in \mathcal{S}_l$ or $\phi_o(\mathbf{X}) = 1, \forall \mathbf{X} \in \mathcal{S}_l$, this leads to $w_i = 0$ in all cases. Hence, the term $\sum_{\mathbf{X}_i \in \mathcal{S}_l} w_i \phi_c(\mathbf{X}_i) = 0$ in Equation (4) in the original Problem 4.1. Therefore, both the initializations separately result in zero (also known as black) images. However, under the gray world assumption such initialization is the farthest possible one, from the gray world. Let $[0, C_{max}]$ be the

		o-0	o-1	o-2	o-3	o-4	r-0	r-1	r-2
ATE RMSE [cm] ↓	w/o TT, HO	70.00	20.09	104.50	34.87	75.78	86.67	65.53	78.25
	w/o HO	40.95	24.25	104.29	56.74	89.74	94.03	87.97	90.66
	w/o TT	2.11	1.49	2.60	26.19	10.82	12.36	9.21	31.68
	Ours	0.59	1.74	1.70	0.81	3.47	4.51	0.91	7.49
Depth L1 [cm] ↓	w/o TT, HO	47.95	29.55	79.91	46.75	55.46	69.54	66.50	64.33
	w/o HO	55.62	28.03	80.33	69.59	55.20	77.24	61.08	63.10
	w/o TT	5.20	2.53	11.15	42.29	23.17	22.83	15.25	39.45
	Ours	3.20	2.15	10.43	11.76	13.23	11.86	4.79	20.95
PSNR [dB] ↑	w/o TT, HO	16.57	23.56	12.26	14.51	15.84	12.47	13.31	15.46
	w/o HO	19.59	22.34	12.41	15.17	14.83	13.07	11.58	15.37
	w/o TT	29.27	31.22	22.21	14.76	19.76	18.82	20.27	19.07
	Ours	30.34	31.67	23.05	23.32	26.19	21.22	26.29	22.54

Table 5. **Ablation Study on the full Replica [35]**. This is the full version of Table 3 on Replica [35] dataset. The best results for each evaluation metric are **bolded**. The proposed components consistently contribute significantly to the ablated baselines.

range of the color c . The gray-world assumption sets the expected value of c to be $C_{max}/2$. However, both initializations lead to $c = 0$, which is the farthest value from $C_{max}/2$, which makes such initialization sub-optimal under the gray-world assumption. In other words, $C_{max}/2$ would have been a better initialization for the made assumption, and any initialization between 0 (representing the zero image) and $C_{max}/2$, would have been better than the zero image. Note that the initializations $\phi_o(X) = 0, \forall X \in \mathcal{S}_l$ or $\phi_o(X) = 1, \forall X \in \mathcal{S}_l$ lead to zero image, making them sub-optimal initializations. ■

Theorem A.5 (Theorem 4.8 in the paper) *The solution to Problem 4.7 will optimize Problem 4.1 without violating the constraints and with the optimal transport for $|\mathcal{S}_o^2| \gg |\mathcal{S}_o^1|$.*

Proof The first part of the proof concerns establishing the relationship between the solution to Problem 4.7 to that of Problem 4.1. In particular, the non-violation of the constraint is addressed. Note that Problem 4.7 imposes the constraint $\phi_o(X) \in \{0, 1\}$ for all $X \in \mathcal{S}_o^1$. The use of these constraints is in fact motivated by the results of Theorem A.3. Since Theorem A.3 assures the validity of the mentioned constraints to Problem 4.1, this part of the proof follows as a direct Corollary from the same.

The second part of the proof makes use of the ordered partition proposed in Theorem A.3. It has been shown that the role of \mathcal{S}_o^2 is irrelevant regarding making any difference to Problem 4.1. It is important to notice that \mathcal{S}_o^2 is a part of the variables being optimized. However, $X \in \mathcal{S}_o^2$ do not contribute to the original problem in any form. When the suggestion of Problem 4.7 on fixing $\phi_o(X) = o_{init}$ for all irrelevant part $X \in \mathcal{S}_o^2$ is considered, it lowers down the fraction of variables to be optimized, and in extreme cases

to zero (or close to zero). When the distributions of $\phi_o(X)$ before and after the optimization are compared, it becomes clear that fixing $\phi_o(X) = o_{init}$ leads to the optimal solution with the optimal transport, for $|\mathcal{S}_o^2| \gg |\mathcal{S}_o^1|$ with sufficiently high $|\mathcal{S}_o^2|$. The transport is minimized by fixing $\phi_o(X)$ for all irrelevant parts $X \in \mathcal{S}_o^2$. ■

Appendix B. Implementation Details

B.1. Feature Grids and Decoders

As mentioned in the main paper, the scene feature grids have 7 hierarchies. We use four feature channels for each hierarchy, with the first three being the color feature channels and the last one being the opacity feature channels.

For the decoders for RGB and opacity, we use two MLPs with three hidden layers. The first two hidden layers have a dimension of 32 with the ReLU activation function, and the last hidden layer has 32 plus extra dimensions from the skipping connections from the input layer, using the Sigmoid function with temperature parameters τ for activation. That is, the final output of the decoder is $\text{Sigmoid}(\tau X)$, where X denotes the output vector of the last layer before the activation. We will discuss in B.3 how we choose the temperature parameter τ .

B.2. Initialization

The loss used in the initialization process is similar to the one used in BA. The whole process can be divided into three stages: (1) In the first 150 iterations, an L1 loss between the rendered depth and constant fake depth 1.5[m] is used, and we only optimize the scene feature grids and the decoders. (2) From the 150th iteration and afterward, $\mathcal{L}_{warping}$ from Eq. 12 is used with sizes $Z = \{1, 7, 11\}$ and scalar 0.1, and we also start optimizing camera poses (3) From the 800th

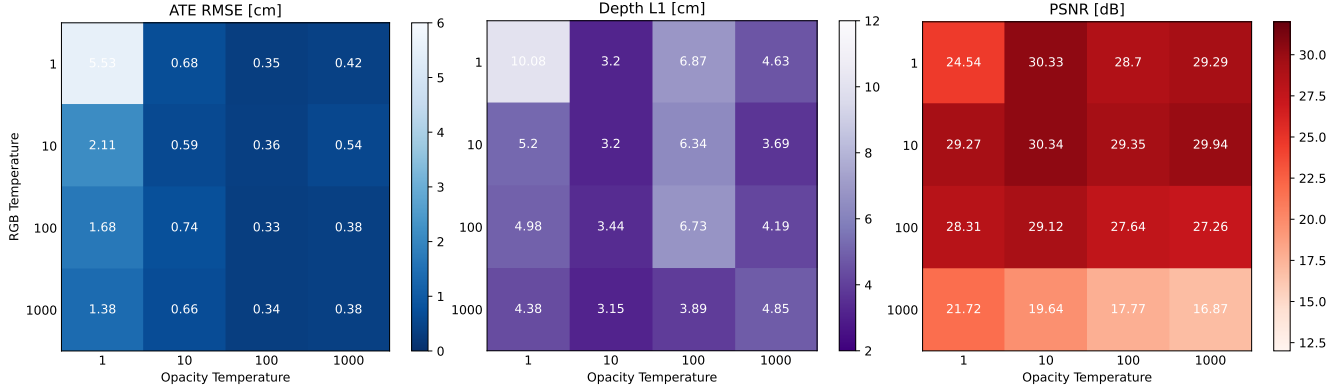


Figure 6. **Tracking and Mapping Performance by Different Sigmoid Temperatures.** Results obtained on Replica [35] office-0. Darker colors indicate better results. These adjustments illustrate the choice of the softly binarized decoders presented in Section 4.

iteration and afterward, \mathcal{L}_{rgb} from Eq. 11 is added to the total loss with scalar 0.5.

B.3. Hyper-parameters.

Learning Rate. For both Replica and 7 Scenes datasets, the learning rates for the 7 layers of multi-resolution voxels are $\{0.001, 0.0008, 0.0007, 0.0005, 0.0004, 0.0003, 0.0002\}$. The learning rates for the two decoders are both set to 0.0001. The learning rates for camera poses are set based on the stage: 0.001 for initialization, 0.0005 for the tracking, and 0.0001 for the following BAs.

Sigmoid Temperature. We denote the temperature parameter of the Sigmoid activation for opacity and RGB as τ_1 and τ_2 respectively. We experiment on different choices of τ_1 and τ_2 on Replica office-0, and choose the best pair based on the results of tracking and mapping. Specifically, we take values from $\{1, 10, 100, 1000\}$, which gives us 16 combinations for τ_1 and τ_2 . The results are shown in Figure 6. In the ATE RMSE heatmap, the column with $\tau_1 = 100$ gives the best results; in both Depth L1 and PSNR heatmaps, the columns with $\tau_1 = 10$ give the best results. We choose $\tau_1 = 10$ in the paper. However, a further division between $\tau_1 = 10$ and $\tau_1 = 100$ can be studied to obtain an optimal τ_1 . Then we take the RGB temperature $\tau_2 = 10$ as it gives the best results in tracking and mapping with $\tau_1 = 10$. In this paper, “no TT” or “without TT” represents not applying ternary-type opacity and corresponds to $\tau_1 = 1$ with $\tau_2 = 10$.

Other Hyper-parameters In BA, the patch sizes in the warping loss $\mathcal{L}_{\text{warping}}$ is $Z = \{1, 7, 11\}$. The scalars in the total loss \mathcal{L}_{BA} are $\alpha_{\text{rgb}} = 0.1$ and $\alpha_{\text{warping}} = 0.5$.

Appendix C. More Results and Insights

C.1. Ablation Study

In Table 5, we show the ablation study results on the whole Replica [35] dataset. Please note that the results reported in Figure 1 and Table 3 (in the main paper), for the office-0, are the representative, reported for simplicity. Here, we have reported the same experiments on all eight sequences of the Replica [35] dataset. This confirms the validity of the proposed method and the significance of the Hybrid Odometry and the Ternary-type prior.

C.2. Opacity and Weights along Rays

To illustrate that Sigmoid temperature adjustment benefits the ternary-type opacity, at the end of the training, we randomly sample a ray and plot the decoded opacity and calculated weights along the ray, with or without the ternary-type opacity, as shown in Figure 7. With the TT opacity, the weights are more concentrated near the depth with a higher peak, whereas without TT opacity, the weights are less concentrated with an apparent non-zero region before the depth, and have a lower peak. The right part of Figure 7 also illustrates how 0-1 opacity before the depth along a ray can help achieve low weights before the depth, and high weights around the depth.

C.3. Opacity Distributions

To further illustrate that Sigmoid temperature adjustment is helping us achieve the ternary-type opacity, we plot the distribution of opacity on points in the 3D space on Replica [35] office-1, where the points are from the centers of finest feature grids and have a total number of about two million. Specifically, we choose temperature parameters for opacity sigmoid functions to be $\tau_1 = 1, 10, 100$ and 1000 while all other settings are the same.

In Figure 8, right after initialization (the first column), there are tall peaks in the histogram plot, which indicates

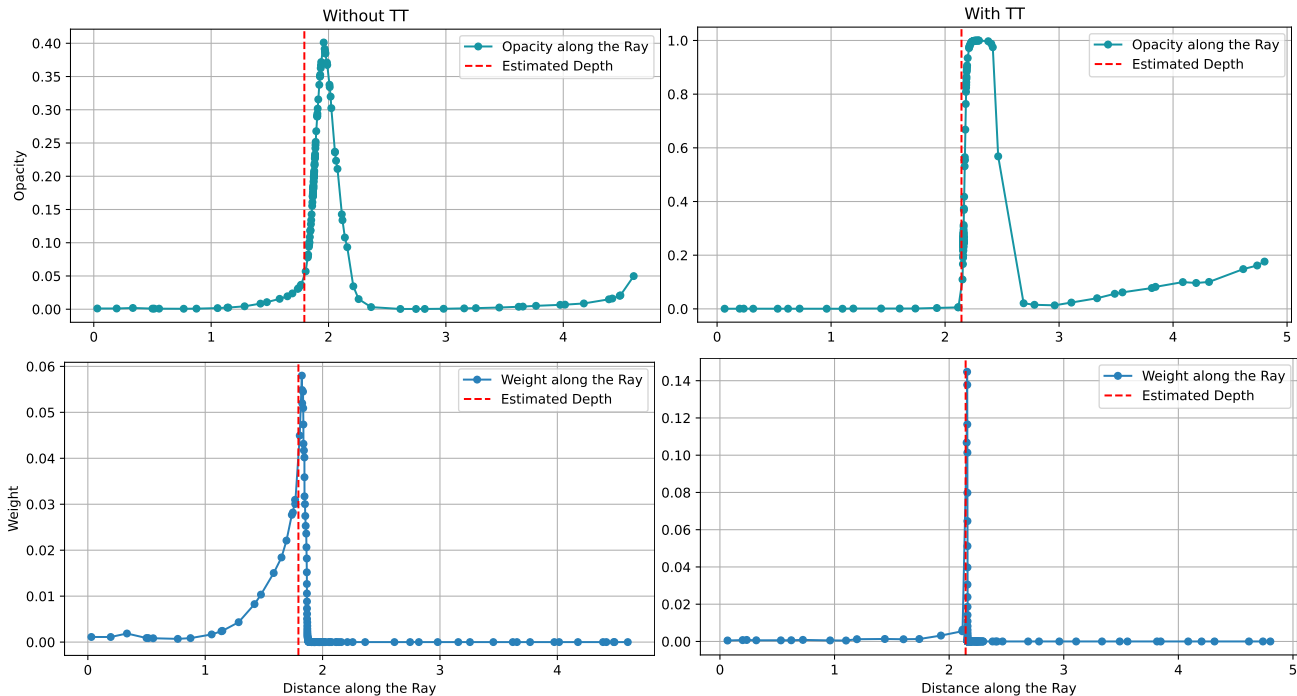


Figure 7. **Opacity and Weights along a Ray.** With the ternary-type opacity (TT), the weights along a randomly sampled ray are more concentrated near the depth with a higher peak. The dots on the curves represent the sampled points on the ray. Data obtained from Replica [35] `office-0` at the end of the training.

that most scene feature grids are not optimized yet, and the opacity values for these peaks are the initial decoded values of opacity. In the middle of the sequence (corresponding to the second column), the last three rows, corresponding to τ_1 value greater than 1, show ternary-type distributions. In the end (corresponding to the third column), $\tau_1 = 10$ aligns best with our prior theorems, where the majority of the grids are still not yet optimized (or only shaking around the initial positions), and there are more feature grids optimized to the opacity of zero than the opacity of one.

C.4. Rendering Visualizations

In Figure 9, we show more visualizations of the rendering results after training the whole sequence. Compared with DIM-SLAM, our method achieves better mapping results with smoother planes. Without any GT depth given for the training, we are able to reconstruct depth maps that are closer to the ground truth.

C.5. Trajectory Visualizations

In Figure 10, we plot the trajectories projected to the x-y plane for the Replica [35] dataset, without scale correction or alignment. For scenes such as `office-4` and `room-2`, compared with DIM-SLAM, the trajectories estimated by our method align better with the ground truth.

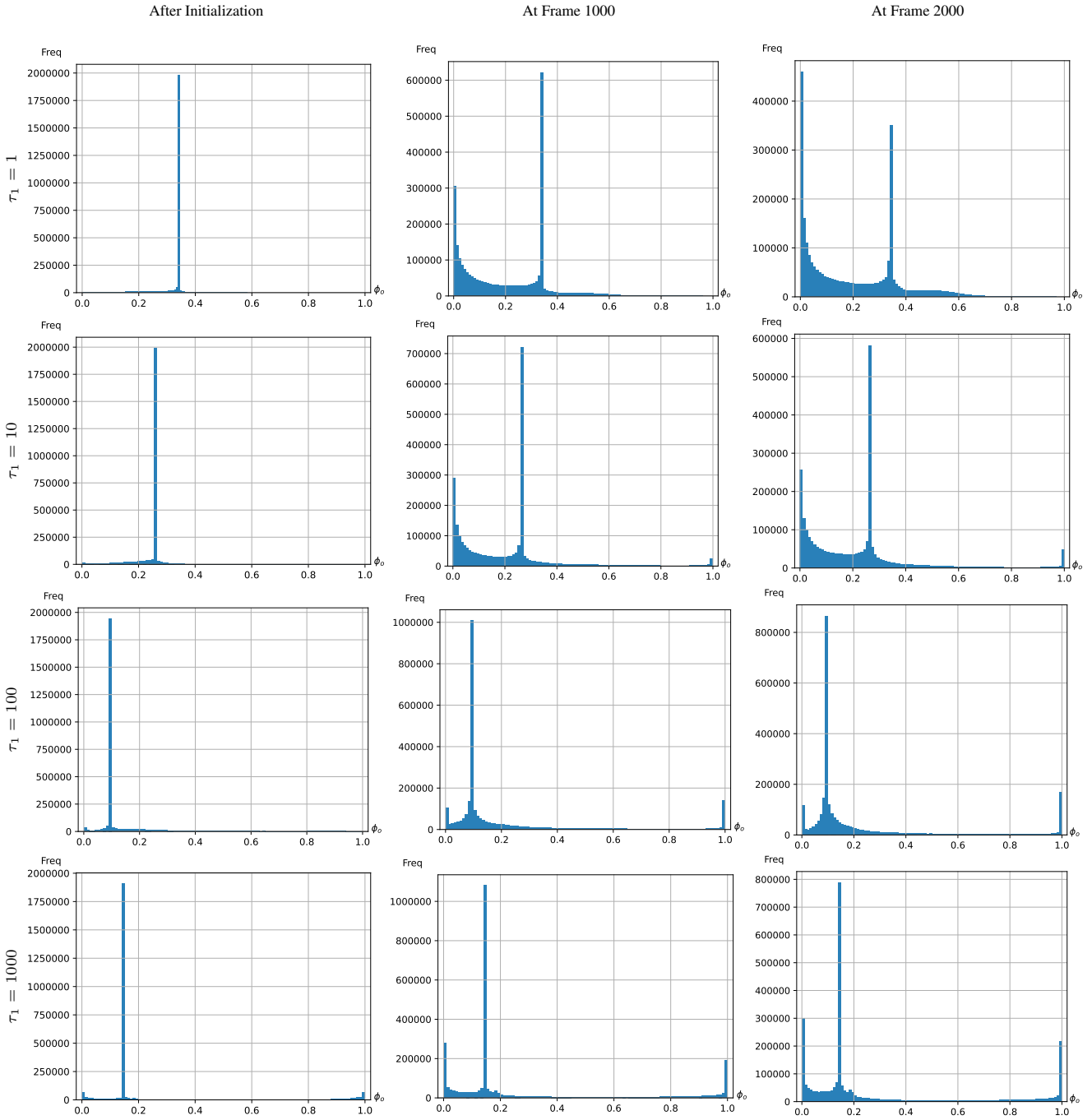


Figure 8. **Opacity Distributions for Different Opacity Sigmoid Temperatures.** The plots are obtained from Replica [35] office-0. The four rows correspond to different temperature parameters of the sigmoid function for opacity, namely $\tau_1 = 1, 10, 100$ and 1000 . The three columns correspond to three stages during the training, namely at the beginning (after initialization), in the middle (at frame 1000), and in the end (at frame 2000).

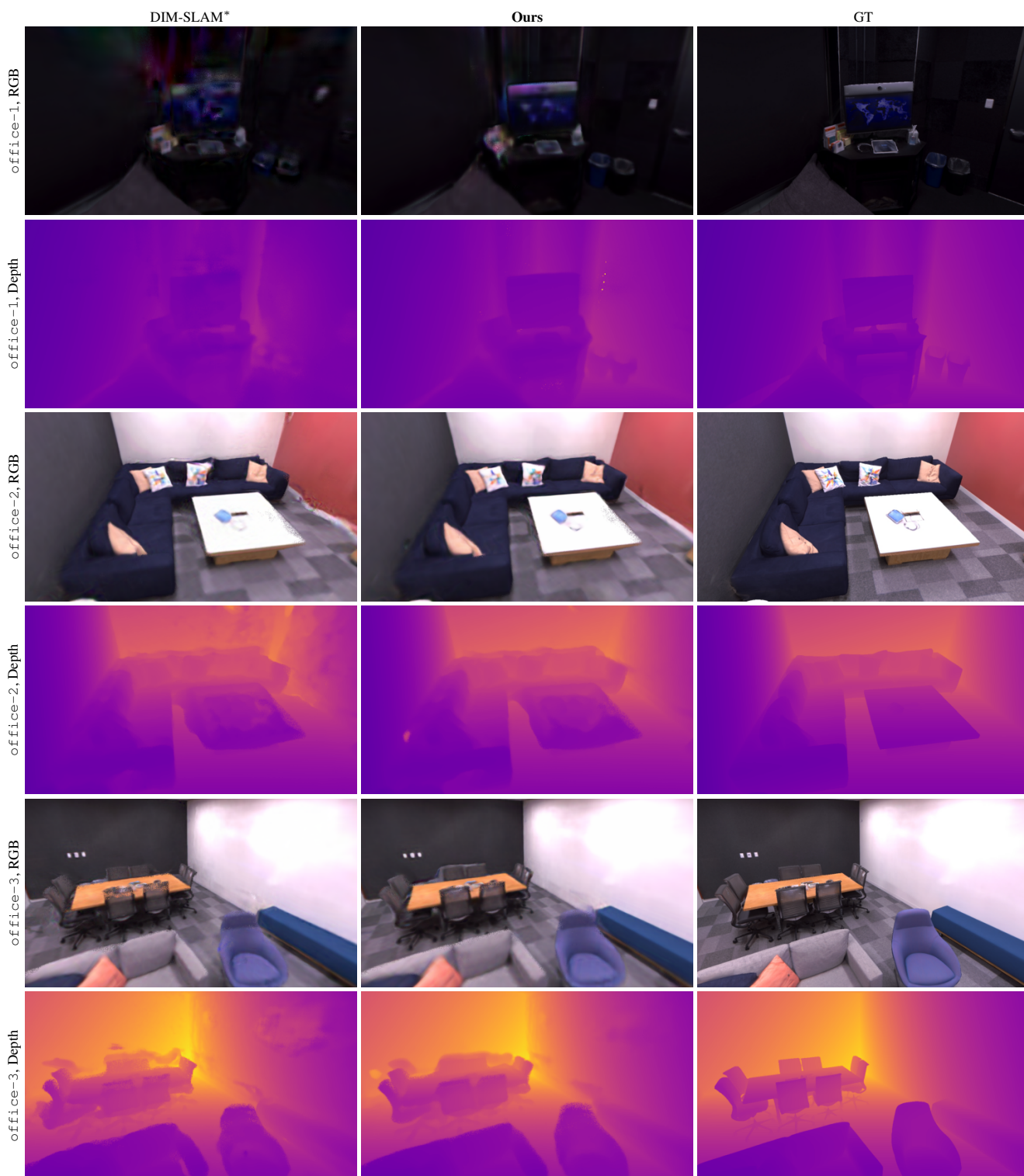


Figure 9. **More Qualitative Results for Rendered RGB and Depth.** We show the rendered RGB and depth from a random pose after training the whole sequence of Replica [35] office-1, office-2, and office-3. DIM-SLAM* refers to our re-implementation for DIM-SLAM [16].

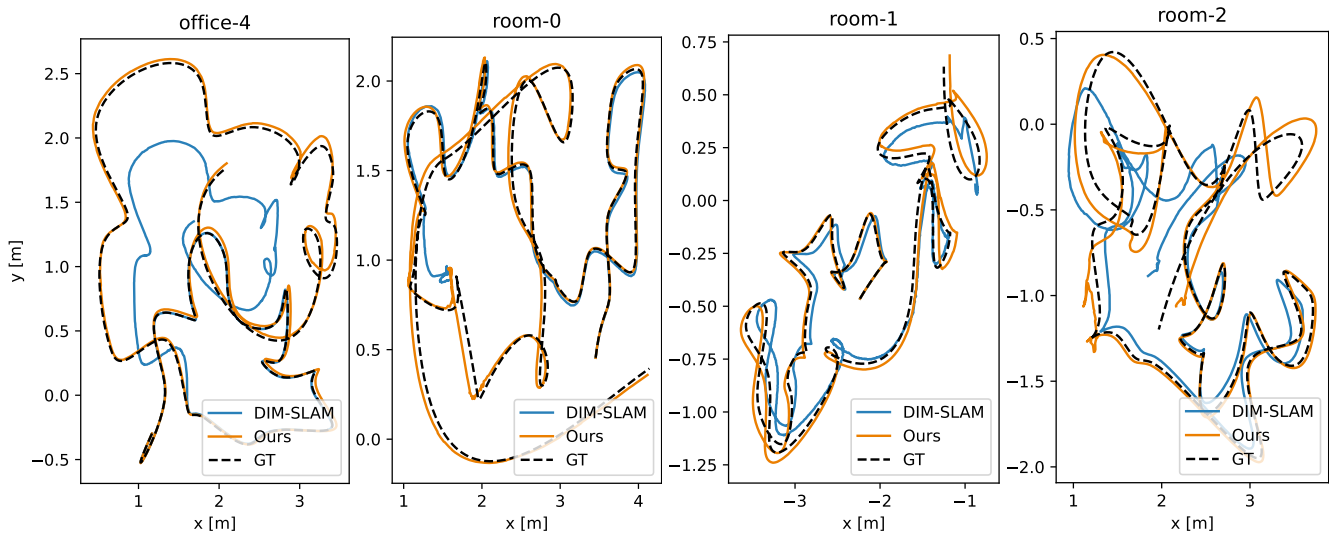


Figure 10. **Trajectory Visualizations on Replica [35]**. The trajectories are projected to the x-y plane, without scale correction or alignment.